Double resonant tunable second harmonic generation in two-dimensional layered materials through band nesting

Sudipta Romen Biswas,[1] Jin Yu ®,[2,3] Zhenwei Wang,[4] Diego Rabelo da Costa,[1,5,6] Chujun Zhao,[6] Shengjun Yuan ®,[4,3] and Tony Low[1,7,*]

[1]*Department of Electrical and Computer Engineering, University of Minnesota, Minneapolis, Minnesota 55455, USA*

[2]*Shanghai Key Laboratory of Mechanics in Energy Engineering, Shanghai Institute of Applied Mathematics and Mechanics, School of Mechanics and Engineering Science, Shanghai University, Shanghai, 200444, China*

[3]*Institute for Molecules and Materials, Radboud University, Heijendaalseweg 135, 6525AJ Nijmegen, The Netherlands*

[4]*Key Laboratory of Artificial Micro- and Nano-Structures of Ministry of Education and School of Physics and Technology, Wuhan University, Wuhan 430072, China*

[5]*Departamento de Física, Universidade Federal do Ceará, Campus do Pici, 60455-900, Fortaleza, Ceará, Brazil*

[6]*Key Laboratory for Micro/Nano Optoelectronic Devices of Ministry of Education, Hunan Provincial Key Laboratory of Low-Dimensional Structural Physics and Devices, School of Physics and Electronics, Hunan University, Changsha 410082, China*

[7]*School of Physics and Astronomy, University of Minnesota, Minneapolis, Minnesota 55455, USA*

We proposed a mechanism to generate giant anisotropic second harmonic nonlinear response via double resonance effect, achieved through band nesting via electronic band-structure engineering. The ideal band setup would be a triplet of nested bands separated by the fundamental resonance energy $\hbar\omega$. We demonstrate theoretically that the proposed phenomenon can be realized in bilayer SnS by band tuning with perpendicular electrical bias, which maximizes the second harmonic susceptibility by several orders of magnitude. Moreover, the tunability of the polarization anisotropy can be useful for realizing novel polarization-sensitive devices.

I. INTRODUCTION

When the electric field intensity is high (on the order of 100 kV/m or more), the materials' response to the field would acquire a notable nonlinear contribution in the electric field [1]. The relation between the electric polarization and the electric-field strength is generally given as [2],

$$P = \varepsilon_0\chi^{(1)}E + \varepsilon_0\chi^{(2)}E^2 + \varepsilon_0\chi^{(3)}E^3 + \cdots$$
$$= P_L + P_{NL}. \quad (1)$$

The first term $\varepsilon_0\chi^{(1)}E$ is the linear polarization, and the higher-order terms generate nonlinear polarization. $\chi^{(n)}$ ($n > 1$) are the nth-order nonlinear susceptibility tensors. For example, $\chi^{(2)}$ is a third rank tensor and relates the second-order nonlinear polarization to the electric-field intensity which is proportional to the square of electric-field strength. Second-order effects consist of the sum frequency generation, where the output frequency is the sum of the two input frequencies, second harmonic generation [(SHG), where the output frequency is twice the input frequency], linear electro-optic effect, optical parametric amplification, etc. [3–5]. Common third-order effects include third harmonic generation, four-wave mixing, optical Kerr effect, two-photon absorption, etc. [6–9]. The study of nonlinear optics began in the 1960s with the first experimental demonstration of SHG

in 1961 [3]. Later, Bloembergen, Boyd, Shen, and co-workers formulated the basic principles of the topic [2,10,11]. These nonlinear effects are typically weak, hence, practical nonlinear optics require bulk materials orders of magnitude larger than the optical path length for the effect to be significant. Recent advent of new nonlinear effects in two-dimensional (2D) atomically thin crystals has shown two to three orders of magnitude larger values of normalized $\chi^{(2)}$, hence, drawing interest from the community [12,13].

In particular, phase mismatch is an important issue in bulk nonlinear optics, when the total phase of the output is not equal to that of its inputs. For SHG, the phase mismatch is described as $\Delta k = 2k_1 - k_2 = 2k(\omega) - k(2\omega)$. The nonlinear output intensity without phase matching (i.e .,$\Delta k \neq 0$) is expressed as [2]

$$I_{2\omega}(L) = \frac{2[\chi^{(2)}]^2\omega_3^2I_1^2(0)}{n_\omega^2 n_{2\omega}\epsilon_0 c^3}L^2 \,\text{sinc}^2\left(\frac{\Delta kL}{2}\right). \quad (2)$$

where the intensity is proportional to the phase-mismatch Δk, input intensity I_1, length of the crystal L, and the SHG coefficient $\chi^{(2)}$. The phase-mismatch factor is maximum when $\Delta kL = 0$. For finite ΔkL, the phase-mismatch factor decreases exponentially and the output intensity is reduced drastically. To satisfy the phase-matching condition ($\Delta k = 0$), the refractive index of the material has to be equal at both the fundamental and second harmonic frequencies i.e., $n(2\omega) = n(\omega)$, which is usually not achievable due to material dispersion. One way to solve this problem is to use

---

birefringent crystals where ordinary and extraordinary waves have different dispersion, and the phase-matching condition can be satisfied [14]. But in this case, the input and output are bound to be orthogonally polarized. Another technique for phase-mismatch correction is called quasi-phase-matching [15,16], which requires complicated setup.

Hence, large $\chi^{(2)}$ and small Δk are necessary for efficient nonlinear optics. In this regard, 2D materials can be advantageous over traditional bulk nonlinear materials. Typically reported $\chi^{(2)}$ in 2D materials such as MoS_2, WSe_2, h-BN, and GaSe [12,17], are two to three orders of magnitude larger than that in prototypical bulk materials (e.g., $LiNbO_3$, Quartz, KDP, BBP, GaAs). For example, $\chi^{(2)}$ of MoS_2 was reported experimentally to be 5×10^3–10^5 pm/V in Ref. [18], whereas $\chi^{(2)}$ of well-known nonlinear material $LiNbO_3$ is $\sim$60 pm/V. The phase mismatch becomes negligible because of the atomic thickness of 2D layers ($\sim$nanometers) compared to bulk materials ($\sim$millimeters) [2,19]. Since nonlinear output intensity is also proportional to the device size (L), a further two to three orders of magnitude increment of $\chi^{(2)}$ in 2D materials is required to compensate for the reduction in device dimensions. In this paper, we present an approach where such giant $\chi^{(2)}$ can be realized through double-resonance effect. This is achieved by electrostatic tuning of the band structure, achieving a triplet of nested bands which allows for resonance with both the ω and 2ω transitions.

In general, nested double-resonant bands should be rare occurrence in pristine 2D materials. Hence, we narrowed our choices to 2D materials with quantum-well-like properties, whose electronic band structures are easily tunable with an out-of-plane electric field [20,21], due to the strong interlayer coupling [22]. We study SnS, a group-IV transition-metal monochalcogenide, which is isoelectronic with the puckered honeycomb structure of black phosphorus (BP) [23] (see Fig. 1). Similar to BP, SnS has anisotropic optical properties (see linear optical properties of bilayer SnS in the Supplemental Material [24] Sec. A, also see the references therein [20,25,26]). Unlike BP, which belongs to D_{2h} point group, SnS has a reduced symmetry (C_{2v} point group) and is noncentrosymmetric for odd-numbered layers [27]. The even-numbered layers retain the inversion center, which can be broken by applying an out-of-plane electric field introduced by modifications of the on-site potentials of the constituent atoms. By tuning the applied perpendicular bias, the band.structure of bilayer SnS, and, therefore, its SHG coefficients can be tuned.

II. THEORY AND APPROACH

In this paper, we focus on the second-order nonlinearity, specifically the SHG. As the second-order nonlinear susceptibility [$\chi^{(2)}(\omega_3; \omega_1, \omega_2)$] (where ω_1, ω_2 are input frequencies, and $\omega_3 = \omega_1 + \omega_2$ is the output frequency) is a third rank tensor, there are 27 different tensor elements for each combination of the input and output frequencies. The number of independent nonzero tensor elements is greatly reduced when symmetry operations are taken into account. Considering permutation symmetry, we can write $\chi_{ijk}^{(2)}(2\omega; \omega, \omega) = \chi_{ikj}^{(2)}(2\omega; \omega, \omega)$, which means that if one permutes the last
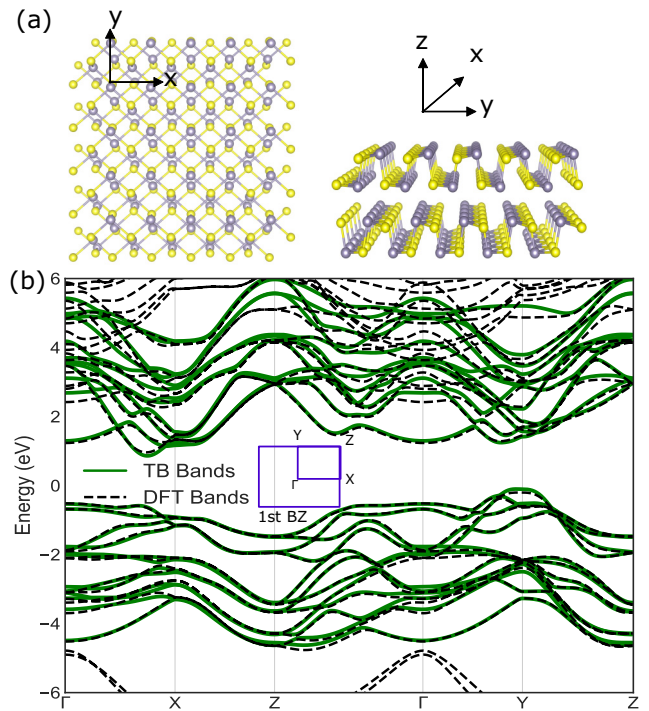
FIG. 1. The top and side views of bilayer SnS atomic structure are shown in (a). Sn and S atoms are indicated by the gray and yellow balls, respectively. Panel (b) shows the band diagram of bilayer SnS where solid (dashed) lines denote the tight-binding (TB) density functional theory (DFT) bands. The rectangular first Brillouin zone is shown in the inset. There is a very good agreement between TB and DFT bands for the low-energy range of interest.

two indices in $\chi_{ijk}^{(2)}$, the value will be the same because the order of the input fields is not important. This reduces the maximum number of nonzero tensor elements from 27 to 18. Crystallographic symmetries can further reduce the number of nonzero tensor elements. For example, there are only seven nonzero independent tensor elements for point-group C_{2v} (xzx, xxz, yyz, yzy, zxx, zyy, zzz) [2]. According to Neumann's principle [28], any physical property of a crystal has to remain invariant after applying symmetry operations belonging to that crystal. However, in centrosymmetric systems, the existence of an inversion center requires polarization to be antisymmetric with an external electric field. For second-order polarization, this is only satisfied when $\chi^{(2)}$ is zero. As a result, all the terms in $\chi^{(2)}$ vanish and these crystals cannot produce any bulk SHG response. It is possible to break the inversion symmetry by applying external stimulus, such as the DC electric field [29–31], DC current [32], strain [33], or structural engineering by patterning nanostructured arrays [34,35]. Thus, tunable nonzero SHG can, in principle, be achieved in centrosymmetric materials.

We use a TB Hamiltonian generated by Wannier interpolation [36,37] from DFT calculations. To construct a reliable TB model for multilayer SnS, we performed first-principles calculations to calibrate the effective Hamiltonian, using the QUANTUM ESPRESSO package [38,39]. Our parametrization procedure in this paper is based on the formalism of maximally localized Wannier functions [40,41] as implemented in

the WANNIER90 code [42]. Ultrasoft Perdew-Burke-Ernzerhof potential [43] was used to describe the exchange interactions with a kinetic-energy cutoff of 60 Ry. A $12 \times 12 \times 1$ Monkhorst-Pack [44] grid was used for the Brillouin-zone sampling for both the relaxation and static calculations. A vacuum thickness of 20 Å was introduced to avoid

spurious interactions between adjacent images in the direction perpendicular to the 2D plane. Diagonalizing the TB Hamiltonian, we get the eigenenergies and eigenfunctions, which are used to calculate the SHG coefficient $\chi^{(2)}$ using the following equations. The total SHG coefficient consists of three terms [45],

$$\chi_{\text{inter}}^{abc}(2\omega; \omega, \omega) = \frac{e^3}{\hbar^2} \sum_{nml} \int \frac{d\mathbf{k}}{4\pi^3} \frac{r_{nm}^a \{ r_{ml}^b r_{ln}^c \}}{\omega_{ln} - \omega_{ml}} \left\{ \frac{2 f_{nm}}{\omega_{mn} - 2\omega} + \frac{f_{ml}}{\omega_{ml} - \omega} + \frac{f_{ln}}{\omega_{ln} - \omega} \right\}, \tag{3a}$$

$$\chi_{\text{intra}}^{abc}(2\omega, \omega, \omega) = \frac{e^3}{\hbar^2} \int \frac{d\mathbf{k}}{4\pi^3} \left[\sum_{nml} \omega_{mn} r_{nm}^a \{ r_{ml}^b r_{ln}^c \} \left\{ \frac{f_{nl}}{\omega_{ln}^2 (\omega_{ln} - \omega)} - \frac{f_{lm}}{\omega_{ml}^2 (\omega_{ml} - \omega)} \right\} \right.$$
$$\left. -8i \sum_{nm} \frac{f_{nm} r_{nm}^a \{ \Delta_{mn}^b r_{mn}^c \}}{\omega_{mn}^2 (\omega_{mn} - 2\omega)} + 2 \sum_{nml} \frac{f_{nm} r_{nm}^a \{ r_{ml}^b r_{ln}^c \} (\omega_{ml} - \omega_{ln})}{\omega_{mn}^2 (\omega_{mn} - 2\omega)} \right], \tag{3b}$$

$$\chi_{\text{mod}}^{abc}(2\omega, \omega, \omega) = \frac{e^3}{2\hbar^2} \int \frac{d\mathbf{k}}{4\pi^3} \left[\sum_{nml} \frac{f_{nm}}{\omega_{mn}^2 (\omega_{mn} - \omega)} \{ \omega_{nl} r_{lm}^a \{ r_{mn}^b r_{nl}^c \} - \omega_{lm} r_{nl}^a \{ r_{lm}^b r_{mn}^c \} \} - i \sum_{nm} \frac{f_{nm} r_{nm}^a \{ r_{mn}^b \Delta_{mn}^c \}}{\omega_{mn}^2 (\omega_{mn} - \omega)} \right]. \tag{3c}$$

Here, $\chi_{\text{inter}}^{abc}$ is the interband contribution, $\chi_{\text{intra}}^{abc}$ is a modification due to intraband motion, and χ_{mod}^{abc} is a modulation of intraband motion by interband polarization energy. r_{nm}^a's are the matrix elements of position operator between bands n, m along the a direction, $f_{nm} = f_n - f_m$ is the difference of Fermi-Dirac factors between bands n, m; ω_{nm} is the energy difference between bands n, m. The band indices n, m, and l runs over all bands. $\{ r_{ml}^b r_{ln}^c \} = \frac{1}{2} (r_{ml}^b r_{ln}^c + r_{ml}^c r_{ln}^b)$ is used to ensure intrinsic permutation symmetry. $\Delta_{mn}^b = v_{mm}^b - v_{nn}^b$, where v_{nm}^b is the velocity matrix element in the b direction given by $v_{nm}^b = i\omega_{nm} r_{nm}^b$.

From an inspection of the terms in the susceptibility equations, we can formulate a criterion for maximizing $\chi^{(2)}$. For example, in Eq. (3a), there are ω and 2ω terms in the denominator. When we have three bands m, l, and n satisfying the condition $\omega_m - \omega_l = \omega_l - \omega_n$, both ω and 2ω terms become resonant. The scenario where the bands are equidistant over some area in the 2D k space (Brillouin zone) is called "band nesting," and the so-called "double resonance" condition [46] is satisfied, rendering significant enhancement of $\chi^{(2)}$.

III. RESULTS AND DISCUSSION

Figure 1 shows the atomic [panel (a)] and electronic [panel (b)] structure of bilayer SnS. The layers are AB stacked, and x and y denote zigzag and armchair directions, respectively. The unit cell consists of four pairs of Sn and S atoms stacked in the AB configuration, which is more favorable in energy than other configurations. The band structure of bilayer SnS is plotted in Fig. 1(b). Our first-principles calculations result shows that it is an indirect gap semiconductor with the valence- band maximum located in the highly symmetric Y point and the conduction-band minimum located between Γ and X points. To construct a reliable TB model, the p_x, p_y, and p_z orbitals of Sn and S are chosen. The band structure derived from the 24-orbital TB Hamiltonian shows that there is a very good agreement between DFT and TB bands, especially in the low-energy region of interest. Since the band structure of

bilayer SnS is well reproduced from the TB model, we can further study the effect of the external electric field on the susceptibility. The calculated $\chi^{(2)}$ parameters in 2D (sheet) units are shown in Fig. 2 as a function of applied perpendicular bias Δ and frequency ω. Temperature T is set to be 300 K, and the electron relaxation parameter which is used to "broaden" the frequency ($\omega \equiv \omega + i\Gamma$) is set to be 10 meV. The out-of-plane electrical bias is introduced by adding a diagonal matrix to the TB Hamiltonian where each diagonal element is the on-site potential of the corresponding atom due to the electric
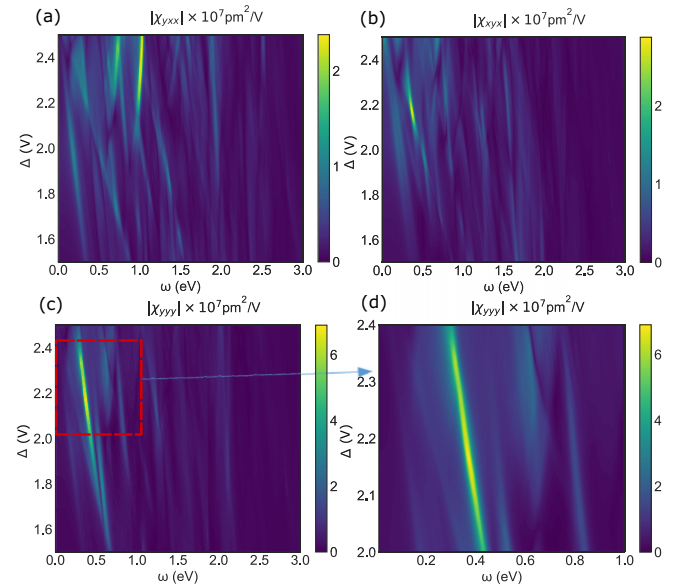
FIG. 2. Three different components of sheet susceptibility $\chi^{(2)}$ are shown. Panels (a)–(c) show χ_{yxx}, χ_{xyx}, and χ_{yyy}, respectively, for bilayer SnS as a function of applied bias Δ and frequency ω. The maximum value of $\chi^{(2)}$ is achieved for χ_{yyy}, $\sim 7 \times 10^7$ pm²/V. The zoomed plot of χ_{yyy} is shown in (d) where a prominent peak occurs for $\Delta \sim 2.16$ V.
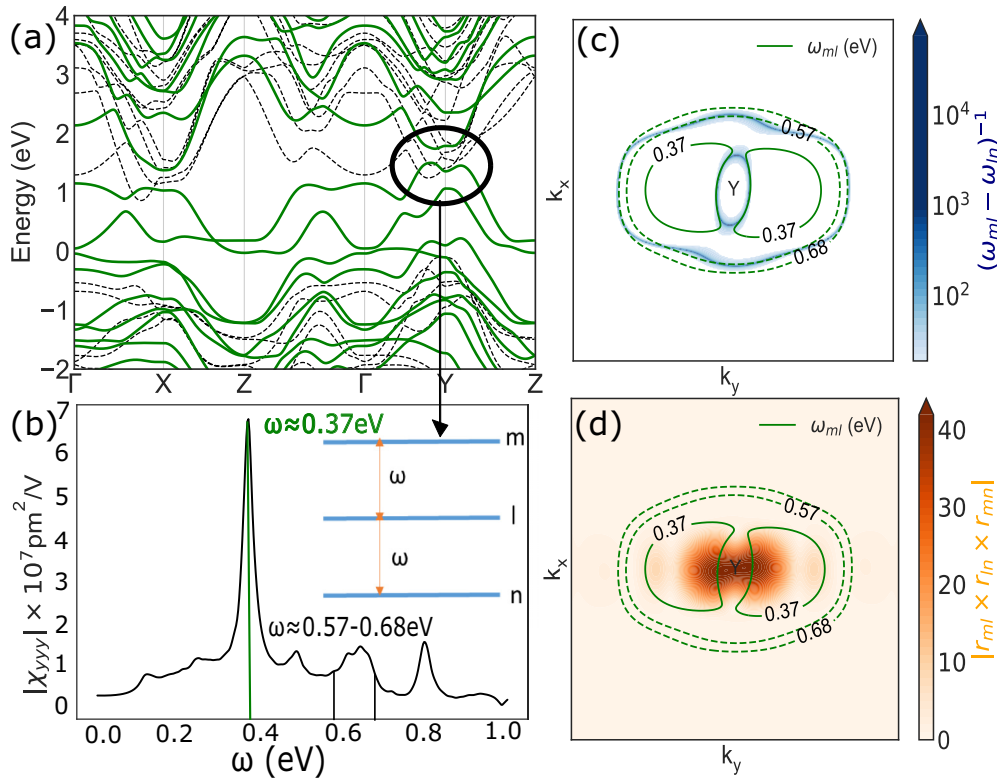
FIG. 3. Schematic of double resonance in bilayer SnS. (a) Band structure of bilayer SnS with/without perpendicular bias of $\Delta = 2.16$ V. The solid (dashed) lines show the biased (unbiased) band structure. Near point Y (circled), top two valence bands (l, n) and bottom conduction band (m) appear to be nested. χ_{yyy} for $\Delta = 2.16$ V is shown in (b). The prominent peak is located at $\omega \simeq 0.37$ eV. In panels (c) and (d), Brillouin-zone contour plots are shown around point Y. The blue contours in (c) show the inverse of energy difference ($\omega_{ml} - \omega_{ln}$) on a logarithmic scale, whereas the orange color in (d) shows the magnitude of matrix element products between the bands. The regions where maximum of these two features overlap are where $\chi^{(2)}$ would be maximum, and the frequency contour that coincides with this region is $\omega_{ml} = 0.37$ eV, which gives a peak SHG frequency of 0.74 eV.

field. There are three independent $\chi^{(2)}$ components for C_{2v} point-group symmetry in 2D: χ_{yyy}, χ_{yxx}, and $\chi_{xyx} = \chi_{xxy}$ [27]. Due to anisotropy, each component has a different maximum amplitude for different bias and frequency. At higher biases, the susceptibility becomes highly nonlinear as function of the bias. The overall maximum amplitude of $\chi^{(2)}$, $\chi^{(2)}_{\max}$, is about $\sim 7 \times 10^7$ pm²/V for the χ_{yyy} component, which corresponds to $\sim 8 \times 10^4$ pm/V in equivalent bulk units. This value of $\chi^{(2)}$ is $\sim$3 orders of magnitude larger than typically reported theoretical values of nonlinear 2D materials. The experimental values of $\chi^{(2)}$ in 2D materials vary a lot across experiments. For example, the value for MoS_2 ranges from 1.2 to 10^5 pm/V, which is a large variation. Factors, such as substrate and sample preparation process, defects, and excitonic effects can influence the measurement [18,47]. The theoretical values calculated within the DFT lie in the middle of this range [17], ($\sim 10^3$ pm/V). Thus, it is more meaningful to compare our calculations with the theoretical values. To draw further comparison, this value of $\sim 8 \times 10^4$ pm/V is higher than reported values in 2D monochalcogenides (GeS, GeSe, SnS, and SnSe) monolayers which goes up to 10^4 pm/V [48]. The required perpendicular bias for $\chi^{(2)}_{\max}$ is $\Delta \sim 2.16$ V, which corresponds to an electric field of 2.5 V/nm, which is smaller than the breakdown electric field of SiO_2 thin films (3 to 4 V/nm) [49]. Accordingly, the corresponding SHG frequency is 0.74 eV.

The SHG enhancement by double resonance is explained in Fig. 3. Figure 3(a) shows the modified band structure of bilayer SnS at bias that yields $\chi^{(2)}_{\max}$, in conjunction with the unbiased band structure. A cutline of χ_{yyy} along $\Delta = 2.16$ V shows the prominent peak at $\omega \simeq 0.37$ eV [Fig. 3(b)]. To explain the double resonance criterion, we identify a set of three bands in the vicinity of the Y point in the Brillouin zone, which is highlighted by the black circle. The relevant band parameters around the Y point are plotted in Figs. 3(c) and 3(d). The quantity $(\omega_{ml} - \omega_{ln})^{-1}$, which quantifies the double-resonance condition, is showed in a logarithmic scale by the blue contours in Fig. 3(c). The orange color in Fig. 3(d) shows the magnitude of the matrix element product between bands m, l, and n in logarithmic scale. In most cases, $\chi^{(2)}$ would be optimal when both these quantities are maximized. To determine the frequency ($\omega_{ml} = \omega$) of this $\chi^{(2)}_{\max}$, we plot contour lines of ω_{ml} in the region of interest. Our result shows that $\chi^{(2)}$ is maximum at $\omega = 0.37$ eV where the solid contour line coincides with the hot spots of these quantities in the momentum space, hence, $\chi^{(2)}$ is maximum at this frequency. Although some of the dashed contours at $\omega \simeq 0.57$–0.68 eV coincide with the double-resonance regions, the matrix elements product along those contours is, at least, two orders of magnitude smaller, which negates the enhancement gained from double resonance. Indeed, we can observe small features in $\chi^{(2)}$ spectra around these frequencies [Fig. 3(b)]. The rest
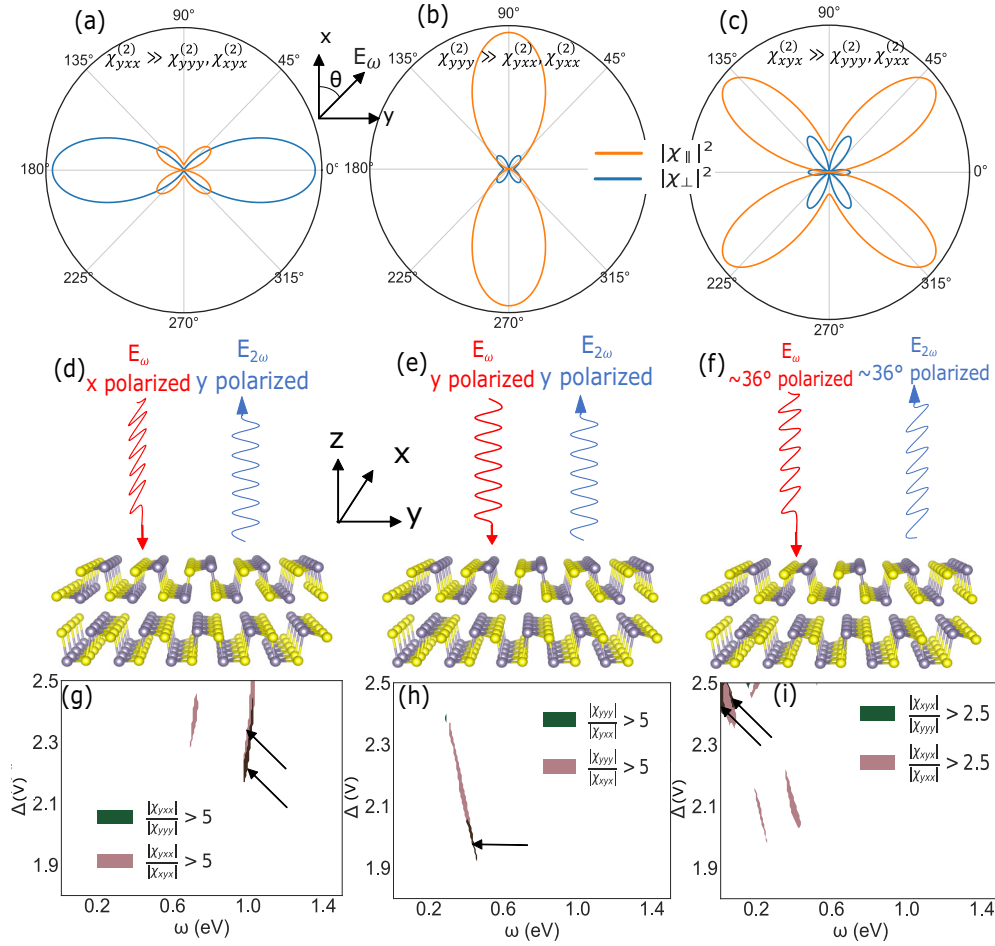
FIG. 4. (a)–(c) show angle-resolved polarization components of $\chi^{(2)}$ ($|\chi_\perp|^2$, $|\chi_\parallel|^2$) as a function of polarization angle θ with respect to the x axis, when one component is much larger than the other two. The effect of having one dominant $\chi^{(2)}$ component is shown in (d)–(f), respectively. For example, in (a) where $\chi^{(2)}_{yxx}$ is dominant, if input is x polarized ($\theta = 0$) the perpendicular SHG component (i.e., y polarized) is maximum, so in (d) the SHG output will be y polarized. Similarly when $\chi^{(2)}_{yyy}$ is dominant (b) and (e), the SHG output will be y polarized with y-polarized input and when $\chi^{(2)}_{xyx}$ is dominant (c) and (f), the SHG output will be maximized with a polarization angle of $\sim 36°$ and for both purely x- and y-polarized light ($\theta = 0, 90°$) the output is much smaller. Panels (g)–(i) show possible regions in the (ω, Δ) space where these conditions can be satisfied. The two different colors show where one $\chi^{(2)}$ component is significantly larger (five times in (g) and (h); 2.5 times in (i); $\chi^{(2)} > 0.5\chi^{(2)}_{\max}$) than the other components. The overlap regions (marked by black arrows) are where the conditions in panels (a)–(c) are satisfied.

of the smaller features seen in $\chi^{(2)}$ are most likely originating from other possible nested trios of bands, albeit with a lesser degree of nesting or smaller matrix element product. SHG response depends on Δ in a highly nonlinear fashion. However, for $\Delta \simeq 0$, SHG scales linearly [31] except near resonant peaks (see the Supplemental Material [24] Sec. B).

Next we turn to the tunability of polarization anisotropy of bilayer SnS. For each crystallographic point group, the effective $\chi^{(2)}$ at an angle of ϕ can be derived from the input field polarization θ and the susceptibility tensor [11],

$$\chi^{(2)}_\phi = \mathbf{e}_\phi \cdot \chi^{(2)} : \mathbf{e}_\theta \otimes \mathbf{e}_\theta.$$

Here, $\chi^{(2)}_\phi$ is the effective SHG coefficient along the ϕ direction, θ is the input field polarization angle, and $\mathbf{e}_\phi$, $\mathbf{e}_\theta$ are the corresponding unit vectors. The SHG output intensity, $I^{2\omega}_\phi \propto |\chi^{(2)}_\phi|^2$. For the C_{2v} point group, the angle-resolved

SHG susceptibilities are given by [27],

$$\chi^{(2)}_\parallel(\theta) = \left(\chi^{(2)}_{xyx} + \chi^{(2)}_{yxx}\right) \sin\theta \, \cos^2\theta + \chi^{(2)}_{yyy} \sin^3\theta,$$
$$\chi^{(2)}_\perp(\theta) = \chi^{(2)}_{yxx} \cos^3\theta + \left(\chi^{(2)}_{yyy} - \chi^{(2)}_{xyx}\right) \cos\theta \, \sin^2\theta. \quad (4)$$

Here, $\chi^{(2)}_{\parallel(\perp)}$ are the parallel (perpendicular) polarization component of the SHG coefficient with respect to the input electric-field (E_ω).

The tunability of SHG components suggests the interesting scenarios where one of the components is dominant over the other two. The angle-resolved polarization components of $\chi^{(2)}$ for these three cases are shown in Figs. 4(a)–4(c), and the corresponding input vs output polarization are illustrated in panels (d)–(f). For example, when $\chi^{(2)}_{yxx}$ is dominant, the perpendicular SHG component, hence, the intensity of the SHG output, is maximum when $\theta = 0$. This means an x-polarized input will result in a y-polarized output, whereas

the output intensity for the other polarization directions will be significantly weaker. Similarly, for dominant $\chi_{yyy}^{(2)}$, when the input is y polarized, the output will be maximized and y polarized. For dominant $\chi_{xyx}^{(2)}$, neither of the x- and y-polarized inputs are converted to strong SHG output. However, the output is maximized with a polarization angle of $\sim 36°$. In Figs. 4(g)–4(i), we analyze the tuning parameter space (ω, Δ) for each of the cases (a)–(c). The two colors show regions where the SHG component is larger by a factor of K [$K = 5$ in panels 4(g) and 4(h); 2.5 in panel 4(i)]. Herein, only the regions where $\chi^{(2)} > 0.5\chi_{max}^{(2)}$ are considered as we are interested in the strong SHG response. The overlap of the two regions indicated by black arrows shows where the component is dominant, and the input-output polarization selectivity is effective. Thus, the tunability of individual SHG parameters allows enhancement of the polarization anisotropy.

In this paper the independent particle approximation (IPA) has been used, and many-body effects, such as quasiparticle self-energy corrections and excitonic effects are not considered. However, in 2D systems, the effects of many-body interactions are expected to be pronounced due to reduced screening effect and quantum confinement [17]. Simple DFT calculations with IPA typically underestimate the band gap measured in optical experiments [50,51]. The quasiparticle band structure using the GW_0 approximation can be calculated by many-body perturbation theory to determine the GW band-gap correction [52,53]. We initially constructed a bilayer-SnS TB model via GW_0 calculations (see Supplemental Material [24] Sec. C, see also the references therein [41,54,55]), to get a more accurate description of quasiparticle energy. But the agreement between TB bands and GW_0 bands was poor with this model. Thus, we decided to use a more complex 24-band TB model that can fit the DFT bands more accurately [see Fig. 1(b)].

For this class of 2D materials, the DFT and GW band structures are similar [27]. To include excitonic effects, first-principles calculations in the Bethe-Salpeter exciton approach [56,57] is extremely computationally challenging as it requires a dense **k**-point grid with thousands of points, and a high number of bands, to achieve a reliable agreement with experiment [17,58]. For nonlinear susceptibility calculations, the complex expressions involving dipole matrix elements of position operators that require nonlocal and frequency-dependent Hamiltonians, make the calculations even more difficult [17,27].

Furthermore, we investigate the effect of perpendicular bias on the band structure, which requires repeating each of these computation-intensive first-principles calculations hundreds of times. The double-resonance effect we discussed here requires very fine tuning of the applied bias, rendering the calculations extremely prohibitive. Also, the SHG response typically increases in the vicinity of exciton peaks when exciton effects are included, and away from the exciton peaks the effects are negligible [59]. Thus, including the excitonic effects would not alter the main conclusion of our paper, which is a giant enhancement of SHG due to double resonance achieved via band tuning. In that regard, our DFT-derived TB approach provides a computationally feasible way to study the proposed effects, which captures the essential physics.

IV. CONCLUSION

The weak nonlinearity in bulk materials is a bottleneck towards realization of efficient nonlinear metasurfaces in low-dimensional systems as the required intensity of input light is too high. There is also the problem of phase mismatch as discussed earlier. Achieving giant nonlinear response in 2D materials can solve both of these problems and facilitate the design of novel nonlinear devices, such as frequency converters, optical modulators, sensors, etc. in small volumes with high conversion efficiency. We proposed a fundamentally new approach to generating giant SHG responses in 2D materials. A tight-binding model for bilayer SnS was formulated to calculate SHG coefficients with a perpendicularly applied electric field. The results demonstrate a giant SHG susceptibility of bilayer SnS up to $\sim 8 \times 10^4$ pm/V which is ~ 3 orders of magnitude larger than typically reported values. We attribute the large SHG enhancement to double resonance, achieved by band nesting. Moreover, the band tunability also allows modification of the existing polarization anisotropy of SHG components. Recent studies [60,61] have reported synthesis and measurement of strong anisotropic- and polarization-dependent SHG in few-layer SnS films. By patterning 2D layers to create plasmonic structures for strong light-matter interaction, further enhancement of nonlinear intensity can be achieved. Furthermore, the polarization anisotropy of SHG can be used to design electrically tunable novel nonlinear polarization-sensitive devices, such as photodetectors, synaptic devices, polarization converters, and switches [48,62,63].

[1] N. Bloembergen, Nonlinear optics and spectroscopy, Rev. Mod. Phys. **54**, 685 (1982).

[2] R. W. Boyd, *Nonlinear Optics* (Academic, San Diego, 2020),

[3] P. Franken, A. E. Hill, C. Peters, and G. Weinreich, Generation of Optical Harmonics, Phys. Rev. Lett. **7**, 118 (1961).

[4] R. Baumgartner and R. Byer, Optical parametric amplification, IEEE J. Quantum Electron. **15**, 432 (1979).

[5] S. Kurtz and F. Robinson, A physical model of the electro-optic effect, Appl. Phys. Lett. **10**, 62 (1967).

[6] P. Maker and R. Terhune, Study of optical effects due to an induced polarization third order in the electric field strength, Phys. Rev. **137**, A801 (1965).

[7] A. Yariv and D. M. Pepper, Amplified reflection, phase conjugation, and oscillation in degenerate four-wave mixing, Opt. Lett. **1**, 16 (1977).

[8] P. Maker, R. Terhune, and C. Savage, Intensity-Dependent Changes in the Refractive Index of Liquids, Phys. Rev. Lett. **12**, 507 (1964).

[9] W. Kaiser and C. Garrett, Two-Photon Excitation in CaF_2:Eu^{2+}, Phys. Rev. Lett. **7**, 229 (1961).

[10] J. Armstrong, N. Bloembergen, J. Ducuing, and P. Pershan, Interactions between light waves in a nonlinear dielectric, Phys. Rev. **127**, 1918 (1962).

[11] Y.-R. Shen, *The Principles of Nonlinear Optics* (John Wiley & Sons, New York, 1984), p. 575.

[12] A. Autere, H. Jussila, Y. Dai, Y. Wang, H. Lipsanen, and Z. Sun, Nonlinear optics with 2D layered materials, Adv. Mater. **30**, 1705963 (2018).

[13] B. Guo, Q.-l. Xiao, S.-h. Wang, and H. Zhang, 2D layered materials: synthesis, nonlinear optical properties, and device applications, Laser Photonics Rev. **13**, 1800327 (2019).

[14] J. Midwinter and J. Warner, The effects of phase matching method and of uniaxial crystal symmetry on the polar distribution of second-order non-linear optical polarization, Br. J. Appl. Phys. **16**, 1135 (1965).

[15] D. Feng, N.-B. Ming, J.-F. Hong, Y.-S. Yang, J.-S. Zhu, Z. Yang, and Y.-N. Wang, Enhancement of second-harmonic generation in $LiNbO_3$ crystals with periodic laminar ferroelectric domains, Appl. Phys. Lett. **37**, 607 (1980).

[16] M. Yamada, N. Nada, M. Saitoh, and K. Watanabe, First-order quasi-phase matched $LiNbO_3$ waveguide periodically poled by applying an external field for efficient blue second-harmonic generation, Appl. Phys. Lett. **62**, 435 (1993).

[17] C.-Y. Wang and G.-Y. Guo, Nonlinear optical properties of transition-metal dichalcogenide MX_2 (M = Mo, W; X = S, Se) monolayers and trilayers from first-principles calculations, J. Phys. Chem. C **119**, 13268 (2015).

[18] N. Kumar, S. Najmaei, Q. Cui, F. Ceballos, P. M. Ajayan, J. Lou, and H. Zhao, Second harmonic microscopy of monolayer MoS_2, Phys. Rev. B **87**, 161403(R) (2013).

[19] D. N. Nikogosyan, *Nonlinear Optical Crystals: A Complete Survey* (Springer, New York, 2005).

[20] T. Low, A. S. Rodin, A. Carvalho, Y. Jiang, H. Wang, F. Xia, and A. H. Castro Neto, Tunable optical properties of multilayer black phosphorus thin films, Phys. Rev. B **90**, 075434 (2014).

[21] T. Low, R. Roldán, H. Wang, F. Xia, P. Avouris, L. M. Moreno, and F. Guinea, Plasmons and Screening in Monolayer and Multilayer Black Phosphorus, Phys. Rev. Lett. **113**, 106802 (2014).

[22] V. O. Özçelik, M. Fathi, J. G. Azadani, and T. Low, Tin monochalcogenide heterostructures as mechanically rigid infrared band gap semiconductors, Phys. Rev. Mater. **2**, 051003(R) (2018).

[23] L. C. Gomes and A. Carvalho, Phosphorene analogues: Isoelectronic two-dimensional group-IV monochalcogenides with orthorhombic structure, Phys. Rev. B **92**, 085406 (2015).

[24] See Supplemental Material at http://link.aps.org/supplemental/10.1103/PhysRevB.107.115409 for linear optical properties of bilayer SnS, SHG coefficients as a function of bias and frequency at low bias, and description of the tight-binding model derived from GW0 calculations. This includes references to P. E Blöochl, Projector augmented-wave method, Phys. Rev. B **50**, 17953 (1994), and G. Kresse and J. Furthmüller, Self-interaction correction to density functional approximation for many electron systems, *ibid.* **54**, 11169 (1996).

[25] D. J. P. de Sousa, L. V. de Castro, D. R. da Costa, J. M. Pereira, Jr., and T. Low, Multilayered black phosphorus: From a tight-binding to a continuum description, Phys. Rev. B **96**, 155427 (2017).

[26] G. Zhang, S. Huang, A. Chaves, C. Song, V. O. Özçelik, T. Low, and H. Yan, Infrared fingerprints of few-layer black phosphorus, Nat. Commun. **8**, 14071 (2017).

[27] H. Wang and X. Qian, Giant optical second harmonic generation in two-dimensional multiferroics, Nano Lett. **17**, 5027 (2017).

[28] F. E. Neumann, *Vorlesungen über die Theorie der Elasticität der festen Körper und des Lichtäthers: Gehalten an der Universität Königsberg* (BG Teubner, Leipzig, 1885), Vol. 4.

[29] K. L. Seyler, J. R. Schaibley, P. Gong, P. Rivera, A. M. Jones, S. Wu, J. Yan, D. G. Mandrus, W. Yao, and X. Xu, Electrical control of second-harmonic generation in a WSe_2 monolayer transistor, Nat. Nanotechnol. **10**, 407 (2015).

[30] J. Klein, J. Wierzbowski, A. Steinhoff, M. Florian, M. Rosner, F. Heimbach, K. Muller, F. Jahnke, T. O. Wehling, J. J. Finley *et al.*, Electric-field switchable second-harmonic generation in bilayer MoS_2 by inversion symmetry breaking, Nano Lett. **17**, 392 (2017).

[31] S. Shree, D. Lagarde, L. Lombez, C. Robert, A. Balocchi, K. Watanabe, T. Taniguchi, X. Marie, I. C. Gerber *et al.*, Interlayer exciton mediated second harmonic generation in bilayer MoS_2, Nat. Commun. **12**, 6894 (2021).

[32] S. Wu, L. Mao, A. M. Jones, W. Yao, C. Zhang, and X. Xu, Quantum-enhanced tunable second-order optical nonlinearity in bilayer graphene, Nano Lett. **12**, 2032 (2012).

[33] S. Rhim, Y. S. Kim, and A. J. Freeman, Strain-induced giant second-harmonic generation in monolayered 2 H-MoX_2 (X = S, Se, Te), Appl. Phys. Lett. **107**, 241908 (2015).

[34] S. Lan, S. Rodrigues, Y. Cui, L. Kang, and W. Cai, Electrically tunable harmonic generation of light from plasmonic structures in electrolytes, Nano Lett. **16**, 5074 (2016).

[35] J. Butet, P.-F. Brevet, and O. J. Martin, Optical second harmonic generation in plasmonic nanostructures: From fundamental principles to advanced applications, ACS Nano **9**, 10545 (2015).

[36] X. Wang, J. R. Yates, I. Souza, and D. Vanderbilt, Ab initio calculation of the anomalous Hall conductivity by Wannier interpolation, Phys. Rev. B **74**, 195118 (2006).

[37] J. R. Yates, X. Wang, D. Vanderbilt, and I. Souza, Spectral and Fermi surface properties from Wannier interpolation, Phys. Rev. B **75**, 195121 (2007).

[38] P. Giannozzi, S. Baroni, N. Bonini, M. Calandra, R. Car, C. Cavazzoni, D. Ceresoli, G. L. Chiarotti, M. Cococcioni, I. Dabo *et al.*, QUANTUM ESPRESSO: A modular and open-source software project for quantum simulations of materials, J. Phys.: Condens. Matter **21**, 395502 (2009).

[39] P. Giannozzi, O. Andreussi, T. Brumme, O. Bunau, M. B. Nardelli, M. Calandra, R. Car, C. Cavazzoni, D. Ceresoli, M. Cococcioni *et al.*, Advanced capabilities for materials modelling with Quantum ESPRESSO, J. Phys.: Condens. Matter **29**, 465901 (2017).

[40] N. Marzari and D. Vanderbilt, Maximally localized generalized wannier functions for composite energy bands, Phys. Rev. B **56**, 12847 (1997).

[41] N. Marzari, A. A. Mostofi, J. R. Yates, I. Souza, and D. Vanderbilt, Maximally localized wannier functions: Theory and applications, Rev. Mod. Phys. **84**, 1419 (2012).

[42] A. A. Mostofi, J. R. Yates, Y.-S. Lee, I. Souza, D. Vanderbilt, and N. Marzari, wannier90: A tool for obtaining maximally-localised wannier functions, Comput. Phys. Commun. **178**, 685 (2008).

[43] J. P. Perdew, K. Burke, and M. Ernzerhof, Generalized Gradient Approximation Made Simple, Phys. Rev. Lett. **77**, 3865 (1996).

[44] H. J. Monkhorst and J. D. Pack, Special points for Brillouin-zone integrations, Phys. Rev. B **13**, 5188 (1976).

[45] J. L. P. Hughes and J. E. Sipe, Calculation of second-order optical response in semiconductors, Phys. Rev. B **53**, 10751 (1996).

[46] L. Nevou, M. Tchernycheva, F. Julien, M. Raybaut, A. Godard, E. Rosencher, F. Guillot, and E. Monroy, Intersubband resonant enhancement of second-harmonic generation in GaN/AlN quantum wells, Appl. Phys. Lett. **89**, 151101 (2006).

[47] L. M. Malard, T. V. Alencar, Ana Paula M. Barboza, K. F. Mak, and A. M. De Paula, Observation of intense second harmonic generation from MoS_2 atomic crystals, Phys. Rev. B **87**, 201401(R) (2013).

[48] Z. Zhang, J. Yang, K. Zhang, S. Chen, F. Mei, and G. Shen, Anisotropic photoresponse of layered 2D SnS-based near infrared photodetectors, J. Mater. Chem. C **5**, 11288 (2017).

[49] C. Sire, S. Blonkowski, M. J. Gordon, and T. Baron, Statistics of electrical breakdown field in HfO_2 and SiO_2 films from millimeter to nanometer length scales, Appl. Phys. Lett. **91**, 242905 (2007).

[50] F. Hüser, T. Olsen, and K. S. Thygesen, Quasiparticle gw calculations for solids, molecules, and two-dimensional materials, Phys. Rev. B **87**, 235132 (2013).

[51] M. Shishkin and G. Kresse, Self-consistent g w calculations for semiconductors and insulators, Phys. Rev. B **75**, 235102 (2007).

[52] M. Shishkin and G. Kresse, Implementation and performance of the frequency-dependent g w method within the paw framework, Phys. Rev. B **74**, 035101 (2006).

[53] H. Wang and X. Qian, Two-dimensional multiferroics in monolayer group iv monochalcogenides, 2D Mater. **4**, 015042 (2017).

[54] R. Elmer, M. Berg, L. Carlen, B. Jakobsson, B. Noren, A. Oskarsson, G. Ericsson, J. Julien, T.-F. Thorsteinsen, M. Guttormsen, G. Løvhøiden, V. Bellini, E. Grosse, C. Müntz, P. Senger, and L. Westerberg, Generalized Gradient Approximation Made Simple, Phys. Rev. Lett. **78**, 1396(E) (1997).

[55] G. Kresse and D. Joubert, From ultrasoft pseudopotentials to the projector augmented-wave method, Phys. Rev. B **59**, 1758 (1999).

[56] E. E. Salpeter and H. A. Bethe, A relativistic equation for bound-state problems, Phys. Rev. **84**, 1232 (1951).

[57] G. Onida, L. Reining, and A. Rubio, Electronic excitations: Density-functional versus many-body green's-function approaches, Rev. Mod. Phys. **74**, 601 (2002).

[58] D. Y. Qiu, F. H. da Jornada, and S. G. Louie, Optical Spectrum of MoS_2: Many-Body Effects and Diversity Of Exciton States, Phys. Rev. Lett. **111**, 216805 (2013).

[59] M. L. Trolle, G. Seifert, and T. G. Pedersen, Theory of excitonic second-harmonic generation in monolayer MoS_2, Phys. Rev. B **89**, 235410 (2014).

[60] M. Zhu, M. Zhong, X. Guo, Y. Wang, Z. Chen, H. Huang, J. He, C. Su, and K. P. Loh, Efficient and anisotropic second harmonic generation in few-layer sns film, Adv. Opt. Mater. **9**, 2101200 (2021).

[61] R. Moqbel, Y.-R. Chang, Z.-Y. Li, S.-H. Kung, H.-Y. Cheng, C.-C. Lee, K. Nagashio, and K.-H. Lin, Wavelength dependence of polarization-resolved second harmonic generation from ferroelectric sns few layers, 2D Mater. **10**, 015022 (2022).

[62] X. Wang, Y. Cui, T. Li, M. Lei, J. Li, and Z. Wei, Recent advances in the functional 2D photonic and optoelectronic devices, Adv. Opt. Mater. **7**, 1801274 (2019).

[63] H. Tian, Q. Guo, Y. Xie, H. Zhao, C. Li, J. J. Cha, F. Xia, and H. Wang, Anisotropic black phosphorus synaptic device for neuromorphic applications, Adv. Mater. **28**, 4991 (2016).